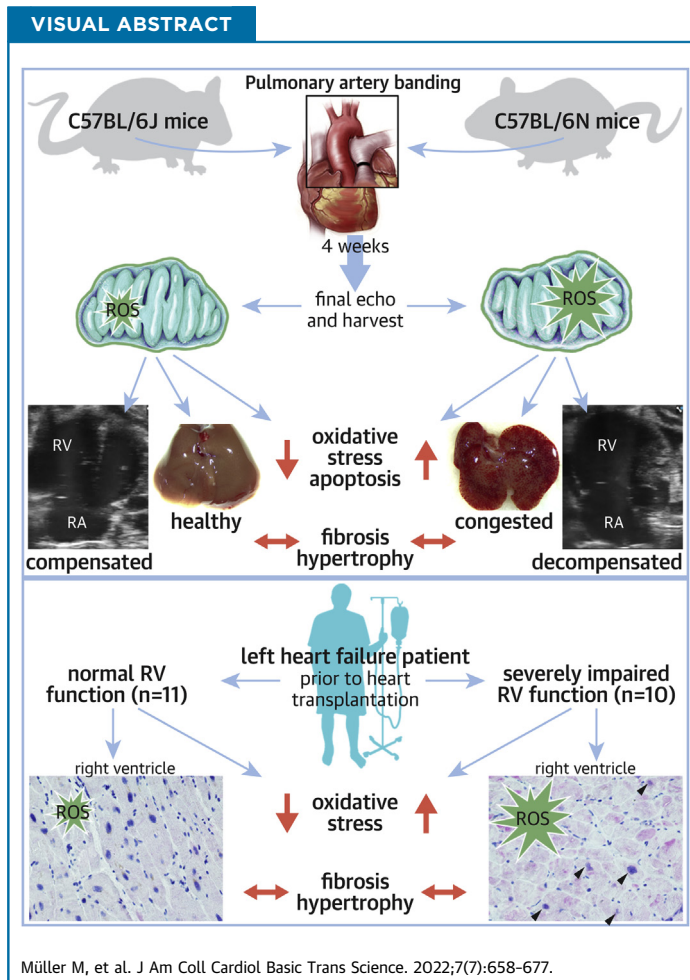


ORIGINAL RESEARCH - PRECLINICAL

Right Heart Failure in Mice Upon Pressure Overload Is Promoted by Mitochondrial Oxidative Stress



Marion Müller, PhD,^{a,b,*} Cornelius Bischof, BSc,^{a,b,*} Torben Kapries, CAND MED,^{a,b} Sophie Wollnitzer, CAND MED,^{a,b} Chiara Liechty, CAND MED,^{a,b} Simon Geißen, CAND MED,^c Torben Schubert, CAND PHD,^{a,b} Dragan Opacic, MD, PhD,^d Muhammed Gerçek, MD,^a Vera Fortmeier, MD,^a Daniel Dumitrescu, MD,^a Uwe Schlomann, PhD,^{a,b} Akylbek Sydykov, MD, PhD,^e Aleksandar Petrovic, CAND PHD,^e Leoni Gnatzy-Feik, CAND PHD,^f Hendrik Milting, PhD,^g Ralph T. Schermuly, PhD,^e Kai Friedrichs, MD,^a Volker Rudolph, MD,^{a,b} Anna Klinke, PhD^{a,b}



SUMMARY

We sought to unravel pathomechanisms of the transition of maladaptive right ventricular (RV) remodeling to right heart failure (RHF) upon pressure overload. Exposure of C57BL/6J and C57BL/6N mice to pulmonary artery banding disclosed a tight relation of structural remodeling with afterload, but a dissociation from RV systolic function. Reduced release of mitochondrial reactive oxygen species in C57BL/6J mice prevented the development of RHF. In patients with left heart failure, increased oxidative damage in RV sections was associated with severely impaired RV function. In conclusion, reactive oxygen species are involved in the transition of maladaptive RV remodeling to RHF. (J Am Coll Cardiol Basic Trans Science 2022;7:658-677) © 2022 The Authors. Published by Elsevier on behalf of the American College of Cardiology Foundation. This is an open access article under the CC BY-NC-ND license (<http://creativecommons.org/licenses/by-nc-nd/4.0/>).

Right ventricular (RV) remodeling following pressure overload, such as in patients with pulmonary hypertension (PH), congenital heart diseases, and secondary to left heart failure (LHF), is characterized by adaptive alterations with right ventricular hypertrophy (RVH) and fibrosis, which can turn maladaptive resulting in RV dilation and deterioration of RV contractility. Right ventricular dysfunction (RVD) increases morbidity and mortality of patients independently of the underlying disease.¹ Among patients with RVD, great variations in the course of the disease exist with long periods of adaptive remodeling with RVH and RV fibrosis on the one hand, and rapid transition to right heart failure (RHF) on the other. The underlying molecular pathomechanisms that determine the deterioration and decompensation of RV function remain scarcely elucidated. For improvement of individual diagnosis and treatment regimen, an understanding of causal pathomechanistic processes is essential. There is great medical need to identify RV-specific therapeutic targets, given that the pathophysiology of RHF and LHF substantially differ, and LHF therapy is ineffective for RHF in most cases.² The animal model of pulmonary artery banding (PAB) is a well-established model of RV pressure overload. However, it is

inconsistently described as a model of compensated RVD and adaptive RVH³⁻⁵ vs RHF.⁶⁻⁹

Some evidence exists that the RV might be particularly prone to oxidative damage, in part because up-regulation of antioxidant enzymes is less effective in RV compared with left ventricular (LV) cardiomyocytes under pathophysiological conditions and because of differences in mitochondrial membrane potentials.¹⁰⁻¹⁶ In fact, oxidative stress, which occurs when levels of reactive oxygen species (ROS) exceed antioxidant capacities, can induce or aggravate detrimental structural and functional myocardial remodeling, such as fibrosis, ion channel dysfunction, capillary rarefaction, dysregulation of excitation-contraction coupling, or mitochondrial dysfunction.^{11,17-19} Mitochondria are among the main sources of ROS in cardiomyocytes. Superoxide anions released from complexes I, II, and III of the electron transport chain are converted to hydrogen peroxide (H₂O₂) by mitochondrial manganese dependent-superoxide dismutase (Mn-SOD, SOD2) and further to H₂O by peroxiredoxin (PRX) and glutathione (GSH) oxidation catalyzed by GSH peroxidase. For regeneration of oxidized PRX and GSH by thioredoxin and GSH reductase, Krebs cycle products as well as the

ABBREVIATIONS AND ACRONYMS

6J = C57BL/6J

6N = C57BL/6N

IRVF = severely impaired right ventricular function

NNT = nicotinamide nucleotide transhydrogenase

nRVF = normal right ventricular function

PAB = pulmonary artery banding

RHF = right heart failure

RVD = right ventricular dysfunction

RVH = right ventricular hypertrophy

TAPSE = tricuspid annular plane systolic excursion

From the ^aClinic for General and Interventional Cardiology/Angiology, Herz- und Diabeteszentrum NRW, University Hospital of the Ruhr-Universität Bochum, Bad Oeynhausen, Germany; ^bAgnes Wittenborg Institute for Translational Cardiovascular Research, Herz- und Diabeteszentrum NRW, University Hospital of the Ruhr-Universität Bochum, Bad Oeynhausen, Germany; ^cDepartment of Cardiology and Cologne Cardiovascular Research Center, University Hospital Cologne, Cologne, Germany; ^dClinic for Thoracic and Cardiovascular Surgery, Herz- und Diabeteszentrum NRW, University Hospital of the Ruhr-Universität Bochum, Bad Oeynhausen, Germany; ^eUniversities of Giessen and Marburg Lung Center, Excellence Cluster Cardio-Pulmonary System, Member of the German Center for Lung Research (DZL), Giessen, Germany; ^fCenter for Molecular Medicine Cologne und Cologne Cardiovascular Research Center, University Hospital Cologne, Cologne, Germany; ^gErich and Hanna Klessmann Institute, Herz- und Diabeteszentrum NRW, University Hospital of the Ruhr-Universität Bochum, Bad Oeynhausen, Germany. *Dr Müller and Mr Bischof contributed equally to this work and are joint first authors.

The authors attest they are in compliance with human studies committees and animal welfare regulations of the authors' institutions and Food and Drug Administration guidelines, including patient consent where appropriate. For more information, visit the [Author Center](#).

reduced form of nicotinamide adenine dinucleotide phosphate (NADPH) are required. In mammalian mitochondria, the oxidoreductase nicotinamide nucleotide transhydrogenase (NNT) can provide NADPH for antioxidant regeneration. It has been disclosed in an animal model of LV pressure overload, that under conditions of enhanced adenosine triphosphate demand but insufficient Ca^{2+} supply, as under pathological increases in mechanical load such as increased afterload, the NNT acts in a reversed mode providing NADH for oxidative phosphorylation at the expense of the NADPH pool.^{18,20} Thus, under these conditions, the antioxidant capacity is diminished and oxidative stress is enhanced. It has not yet been investigated whether this mechanism occurs similarly in the RV. Of note, C57BL/6J (6J) mice, which are the most commonly used mice in cardiovascular research, exhibit an in-frame 5-exon deletion leading to complete absence of NNT protein (*Nnt^{T/T}*).^{21,22} Previously, this sequence variation was linked to impaired glucose tolerance in 6J mice. This is in contrast to C57BL/6N (6N) mice (*Nnt^{+/+}*). Under LV pressure overload, cardiomyocyte mitochondrial ROS generation was higher in 6N mice compared with 6J mice because of the NNT reversed mode.¹⁸

Herein, we aimed to enhance the understanding of pathomechanisms driving the transition from RVD to RHF. We provide an in-depth characterization of the PAB model, present a systematic investigation of cardiac phenotypic and molecular differences between 6J and 6N mice under RV pressure overload, and further elucidate the role of oxidative stress for RHF. In addition, we provide a translational approach by analyzing RV tissue of patients undergoing heart transplantation.

METHODS

CHEMICALS. Chemicals were purchased from Sigma-Aldrich (Darmstadt, Germany), unless otherwise indicated.

ANIMALS. Male C57BL/6J and C57BL/6N mice were purchased from Charles River and Janvier Labs. Mice were housed for at least 1 week to acclimatize to laboratory conditions before starting any experimental procedure. They were kept in a 12:12 hours inverse light cycle and fed a standard rodent diet.

All animal studies were approved by the local animal care and use committees (Ministry for Environment, Agriculture, Conservation and Consumer Protection of the State of North Rhine-Westphalia; State Agency for Nature, Environment and Consumer Protection, NRW, Germany) and followed guidelines from Directive 2010/63/EU of the European

Parliament on the protection of animals used for scientific purposes.

ANIMAL EXPERIMENTAL PROTOCOLS. A titanium clip was placed to the pulmonary artery (PA) between arterial root and bifurcation. The clip diameter was 450 μm (26-gauge), 350 μm (28-gauge), or 300 μm (30-gauge) as indicated, respectively. For final organ harvest, blood was drawn by apical puncture and the heart was excised and flushed with saline. Atria were removed, and the RV was separated from LV and septum, weighed, and processed for further analysis. The liver was excised and processed for histology.

For further details, see the [Supplemental Methods](#).

mitoTEMPO TREATMENT. Where indicated, mitoTEMPO was administered with ALZET micro-osmotic pumps (0.7 mg/kg bw/d, Model 1004, ALZET) over 4 weeks starting directly after PAB surgery. Ultrasound was performed 2 and 4 weeks after surgery, as described in the following text. Final organ harvest was carried out as described in the previous text.

EXPERIMENTAL ECHOCARDIOGRAPHY. Cardiac ultrasound was carried out with a Vevo 3100 Imaging System (FUJIFILM Visualsonics, Inc) using a MX550D Transducer (25-55 MHz, FUJIFILM Visualsonics, Inc). Mice were anaesthetized with isoflurane inhalation (1.5%-2%) and placed in supine position on a heating pad. Electrocardiogram was obtained with integrated electrodes. Body temperature was monitored using a rectal probe ($T = 36.5\text{-}37.5\text{ }^{\circ}\text{C}$). Respiration rate (80-120 breaths/min) was controlled by adjusting depth of anesthesia. A standardized workflow was followed as stated in the position paper of the Working Group on Myocardial Function of the European Society of Cardiology.²³ RV function was assessed and imaged as described by Kohut et al.²⁴ In brief, 2-dimensional recordings of brightness(B)- and motion(M)-mode of parasternal long-axis and parasternal short-axis, respectively, were acquired for analysis of LV parameters. The constriction of the PA was verified in parasternal short-axis at the level of the aortic valve by using the pulse wave Doppler mode. Tricuspid annular plane systolic excursion (TAPSE) and fractional area change (FAC) of the RV and right atrial (RA) area were obtained from the apical 4-chamber view. To assign right ventricular wall thickness (RVWT) and right ventricular internal diameter (RVID), a modified parasternal short-axis view was performed. The mice were tilted laterally to obtain a cross-sectional view from the right hemithorax. The RV was visualized anterior to the LV, and parameters were gathered from M-mode.²⁵

STRAIN ANALYSES. The strain analysis was carried out by the Vevo strain analysis module of the Vevo

Lab analysis software version 3.2.0 (FUJIFILM Visu-sonics, Inc). Strain determines the deformation of the myocardial wall and thereby reflects cardiac function. The analysis uses 2-dimensional speckle tracking calculating the distance a speckle moves between 2 consecutive frames, which is indicated as displacement. The velocity is the displacement per unit time in 3 planes. The longitudinal strain is a dimensionless parameter and shows the tangential movement based on the traced border normalized towards baseline. The software uses the Lagrangian Strain algorithm, which is based on the following formula: $S(t) = [L(t) - L(0)]/L(0)$; with $S(t)$ indicating strain value at a specific time point t ; $L(t)$, length at a specific time point t ; and $L(0)$, length at the start point 0. The analysis was performed by using 3 cardiac cycles of recordings of the apical 4-chamber view. Next, an upward curve including approximately 50% of the RV free wall, the cardiac apex, and 50% of the septal wall was traced. The global longitudinal strain was calculated by applying the strain formula to the entire length of the traced line (myocardial border). To determine the strain of the RV free wall, the segmentation curves were used. At the end of diastole, the anterior and posterior regions were divided into 3 segments equal in length. Each of the 6 segments contain 8 equally spaced points, resulting in 48 points in total. These points (speckles) were used by the algorithm. The average strain curves of the 3 posterior segments are defined as strain values of the RV free wall ($RV_{\text{free wall}}$).

PATIENT STUDY. Patients, who were diagnosed for dilated cardiomyopathy (DCM) and underwent heart transplantation (HTx) at our center between 2015 and 2020 were retrospectively enrolled and included in a case-control study. Written informed consent was acquired according to the “Process instructions for the extraction, collection and storage as well as the use of sample materials from the biomaterial banks of the HDZ NRW for biomedical research purposes, version 3.0 from 04.10.2013,” and the study was conducted according to the Declaration of Helsinki. Patients who underwent mechanical ventricular assist device implantation before HTx were excluded. Functional LV and RV parameters were assessed from routine echocardiography and right heart catheterization between 1 to 8 weeks before HTx surgery. Patients were classified into normal right ventricular function (nRVF) (defined as TAPSE ≥ 16 mm) and severely impaired right ventricular function (iRVF) (defined as TAPSE ≤ 13 mm) groups. Patients with intermediately impaired RV function (TAPSE of 14 and 15 mm) were excluded. Two patients, for whom

TAPSE was not available, were assigned to nRVF according to FAC >35 . Furthermore, standardized right heart catheterization was performed in the context of routine clinical assessment 1 to 8 weeks before HTx. Mean PA pressure was measured in the central PA with a Swan-Ganz catheter. PA wedge pressure was measured by forwarding the Swan-Ganz catheter with the tip balloon inflated from the central PA into the periphery until the balloon completely occluded the particular vessel. Zero reference level for all pressure measurements was set at the mid-thoracic level in all patients. Explanted hearts were dissected, and tissue from predefined RV areas was fixed in 4% formalin at the day of explantation and processed for further analysis as described in the following text. Patient characteristics are listed in [Table 1](#).

HISTOLOGY OF RV SECTIONS. Formalin-fixed, paraffin-embedded RV were cut to sequential 5- μm cross-sections (30 sections in 5 sequential levels, distance between levels was 200 μm). Sections were stained with picosirius red (Polyscience Inc) following standard protocols. Images were acquired with a BZ9000 microscope (Keyence), and picosirius red positive area was quantified in a minimum of 3 sections of 2 levels each, using the ImageJ hue threshold method.

HISTOLOGY OF MURINE LIVER SECTIONS. Formalin-fixed, paraffin embedded livers were cut to 5- μm sections and were stained with hematoxylin/eosin (Dako/Agilent, Waldeck) following standard protocols. Images were acquired with a BZ9000 microscope, and pale purple areas indicating alterations caused by venous congestion were quantified using Keyence BZ2-Analyzer software.

IMMUNOHISTOCHEMISTRY AND IMMUNOFLUORESCENCE. Formalin-fixed, paraffin-embedded RV were cut to sequential 5- μm cross-sections (30 sections in 5 sequential levels, distance between levels was 100 μm). For analysis of cardiomyocyte hypertrophy and capillary density, sections were incubated with Alexa Fluor 594-conjugated wheat-germ agglutinin (Thermo Fisher Scientific) and Alexa Fluor 488-conjugated-isolectin from *Griffonia simplicifolia* (GSI-B4, Thermo Fisher Scientific). For analysis of 8-hydroxy-deoxyguanosine (8-OHdG), rabbit IgG to 8-OHdG (Thermo Fisher Scientific) was used. Apoptotic nuclei were identified by terminal deoxynucleotidyl transferase-mediated dUTP Nick End labeling (TUNEL) method using the In situ Cell Death detection kit (Merck).

For further details see the [Supplemental Methods](#).

IMMUNOBLOT. For protein extraction, frozen heart tissue samples were collected in Precellys ceramic kit

TABLE 1 Patient Characteristics

	nRVF (n = 11)	iRVF (n = 10)
Age, y	53.7 ± 14.7	49.5 ± 14.3
Female/male	3 (27.3)/8 (72.7)	4 (40)/6 (60)
BMI, kg/m ²	26.0 ± 3.7	25.9 ± 3.8
Etiology of DCM		
Genetic	1 (9)	2 (20)
Myocarditis	2 (18.2)	3 (30)
Other	8 (72.8)	5 (50)
Smoking	5 (45.5)	1 (10)
Hypertension	6 (54.6)	5 (50)
Peripheral artery disease	0	0
Stroke	0	0
Diabetes mellitus	2 (18.2)	4 (40)
Renal insufficiency (GFR categories ≥G3b)	2 (18.2)	4 (40)
Chronic obstructive pulmonary disease	0	0
Previous myocardial infarction	0	0
Prior percutaneous coronary intervention	0	0
Prior cardiac surgery	1 (9.1)	0
Atrial fibrillation	4 (36.4)	4 (40)
Permanent pacemaker	2 (18.2)	0
CRT implanted	6 (54.6)	5 (50)
Medication		
Diuretics	10 (90.9)	10 (100)
Beta-blockade	8 (72.7)	9 (90)
ACE-I, ARB	7 (63.6)	9 (90)
Valsartan/sacubitril	4 (36.4)	2 (20)
Ivabradine	1 (9.1)	1 (10)
Marcumar	4 (36.4)	6 (60)
NOAC	1 (9.1)	1 (10)
Glucocorticoid	2 (18.2)	1 (10)
Tacrolimus	1 (9.1)	1 (10)
Statin	3 (27.3)	1 (10)

Values are mean ± SD or n (%). Statistical significance was calculated for numerical data using 2-tailed unpaired Student's *t*-test and for categorical data using Fisher exact test. No statistical differences were observed.

ACE-I = angiotensin-converting enzyme inhibitor; ARB = angiotensin receptor blocker; BMI = body mass index; GFR = glomerular filtration rate; iRVF = severely impaired right ventricular function; NOAC = novel oral anticoagulant; nRVF = normal right ventricular function.

tubes (1.4 mm, 2.0 mL) containing 150 µL ice-cold NP-40 lysis buffer (50 mmol/L Tris-HCL pH 8.0, 137 mmol/L NaCl, 10% Glycerol, 1% NP-40, 2 mmol/L EDTA), supplemented with protease inhibitors, and homogenized using Precellys 24 tissue homogenizer (Bertin instruments). After repetitive vortexing and centrifugation, supernatants were collected. Protein concentrations were determined using Pierce BCA Protein Assay Kit (Thermo Fisher Scientific). Equal amounts of protein from each sample were separated on SDS-polyacrylamide gels and transferred to nitrocellulose membranes (Bio-Rad Laboratories, Inc). The amount of hyperoxidized PRX was detected using an antibody to PRX sulfenic and sulfonic acid at Cys51 (#LF-PA0004, AbFrontier) normalized to cyclooxygenase IV (COX IV, #4844, Cell Signaling)

and densitometrically evaluated using INTAS ECL CHEMOSTAR (INTAS) with rolling ball background reduction.

QUANTITATIVE REAL TIME PCR. Total mRNA was isolated from murine frozen tissues using the miR-Neasy Micro Kit (Qiagen) following the manufacturer's standard protocol. Reverse transcription was performed for 30 min at 42 °C using dNTP Mix (10 mmol/L each, VWR) and SuperScript II Reverse Transcriptase (Thermo Fisher Scientific). qPCR was carried out on StepOnePlus (Applied Biosystems) using Maxima Probe/ROX qPCR Master Mix (Thermo Fisher Scientific) and $2^{-\Delta\text{CT}}$ was calculated. For detecting mitochondrial copy number, quantitative real time PCR on DNA level was performed. Total DNA was isolated from murine frozen tissues using the Pure Link Genomic DNA Kit (Life Technologies) (Qiagen, Hilden, Germany) following the manufacturer's standard protocol. RT-PCR was carried out on StepOnePlus (Applied Biosystems) using Hot-StarTaq DNA Polymerase (Qiagen) according to the manufacturer's instructions. Three specific primer sequences targeting mitochondrial DNA (mtDNA) were analyzed. $2^{-\Delta\text{CT}}$ was calculated, and mtDNA copy number was shown as fold change normalized to the average of expression in 6J mice.

For further details see the [Supplemental Methods](#).

STATISTICS. All data are shown as mean + SD or estimated mean ± SEM if the mixed model was used. The sample size is listed as N. Statistical differences were determined by using GraphPad Prism version 5.0 for Windows. Data were tested for normality using the Kolmogorov-Smirnoff test. For multiple independent groups, 1-way analysis of variance followed by Bonferroni's post hoc test for parametric data, and Kruskal-Wallis test followed by Dunn's multi-comparison test for nonparametric data were used. For within-group comparisons over time, a marginal linear mixed effect model with Bonferroni's post hoc test was used. Fixed variables were timepoint, strain type, and interaction, whereas the individual animal was included as a random variable. For comparisons of 2 independent groups, 2-tailed unpaired Student's *t*-test for parametric data and Mann-Whitney *U* test for nonparametric data were employed. The Kaplan-Meier method was used to present the survival between the groups, whereas the log-rank test was used to compare the curves. The Pearson's correlation was used to test for linear trends. To calculate cutoff points, the logistic regression method of a receiver-operating characteristics curve was employed using the Youden's index ($J = \text{sensitivity} + \text{specificity} - 1$). Categorical data are presented as counts and (%) and

compared with the Fisher exact test. *P* values <0.05 were considered statistically significant. Unless otherwise stated, the significances are given as comparison to the respective control data. In detail, **P* < 0.05; ***P* < 0.01; and ****P* < 0.001.

RESULTS

RV REMODELING IS GRADUALLY AGGRAVATED WITH INCREASING PA CONSTRICTION. In the widely used wild-type mouse strain 6J, PAB with increasing PA stenosis grades of mild, moderate, and severe was applied (Figure 1A). The position of the clip was verified by color Doppler ultrasound (Figure 1B). Whereas mild stenosis did not induce RVH after 2 weeks, moderate and severe PAB provoked a correspondent rise in RVH, reflected by Fulton index and echocardiographically determined diastolic RVWT (Figure 1C). In contrast, RV dilation, as reflected by diastolic RVID, significantly increased to the same extent with mild and moderate stenosis and was even more enlarged upon severe stenosis (Figures 1D and 1E). Similarly, RA area was slightly increased upon mild and moderate stenosis and was considerably more enlarged upon severe stenosis (Figures 1F and 1H), indicating profoundly higher RV pressure. This was corroborated by a higher rate of paradoxical septal motion upon severe stenosis (Figure 1G). Tricuspid annular plane systolic excursion (TAPSE), mirroring RV systolic function, declined with increasing stenosis grade (Figure 1I). Along the lines of RVH, mRNA expression of genes encoding for atrial and brain natriuretic peptides and the relation of myosin heavy chains alpha/beta (MYH6/MYH7), which represent the cardiac fetal gene program that is activated during cardiac hypertrophy, was not significantly altered upon mild but was upon moderate and severe PA stenosis (Supplemental Figure S1A). Also, congruent with RVH and fetal gene reprogramming, interstitial RV fibrosis increased upon 2 weeks of moderate and severe PAB (Supplemental Figures S1B to S1D) and capillary density slightly decreased (Supplemental Figures S2A and S2C). The cross-sectional area of cardiomyocytes was slightly increased after mild PAB, and tended to progressively decrease with severity of PAB (Supplemental Figures S2A and S2C), in accordance with previous findings.⁹

NNT DEFICIENCY PROTECTS FROM RHF UPON PRESSURE OVERLOAD. In contrast to 6J mice, which exhibit a sequence variation leading to absence of the mitochondrial transhydrogenase NNT,^{22,26} 6N mice express NNT (Figure 2A). It has been described before for the LV that under pressure overload, NNT in

cardiomyocytes acts in a reversed mode,¹⁸ as schematically demonstrated in Figure 2B. After 2 and 4 weeks of severe PAB (Figure 2C), no significant differences in RVH were detected between 6J and 6N mice, except a lower RVWT after 2 weeks of PAB in 6N mice (Figure 2D). Accordingly, markers of fetal gene reprogramming were not significantly different between the 2 strains (Supplemental Figure S3). In contrast, RV dilation was markedly enhanced in 6N compared with 6J mice (Figure 2E), accompanied by a significantly more increased RA area in 6N mice after 2 and 4 weeks of severe PAB (Figure 2F). Both parameters showed significant negative correlations with TAPSE (Supplemental Figure S4). Importantly, systolic function was significantly more impaired in 6N compared with 6J mice 2 and 4 weeks after PAB (Figure 2G). Of note, FAC, which is a commonly used parameter of RV systolic function, was confounded in PAB-exposed 6J and 6N mice because of considerable paradoxical septal motion (Supplemental Figures S5A to S5G), which was more pronounced in 6N than in 6J mice (Supplemental Figure S5F). This effect furthermore resulted in a stronger decrease of the LV end-diastolic volume in 6N compared with 6J after 4 weeks of PAB (Supplemental Figure S6A), whereas the LV ejection fraction and LV wall thickness remained unchanged (Supplemental Figure S6B). From the echocardiographic recordings, longitudinal strain analyses were performed using speckle tracking technique to confirm and expand the data on RV function (Figures 2H and 2J). It disclosed that after 4 weeks of severe PAB, longitudinal strain (Figure 2K) and longitudinal displacement and velocity of the RV free wall (Figures 2L and 2M) were significantly diminished in 6N compared with 6J mice after 4 weeks of PAB, indicating impaired RV function. Longitudinal strain parameters significantly correlated with TAPSE (Figure 2N, Supplemental Figure S7A). Analysis of longitudinal displacement, velocity, and strain of combined RV free wall with interventricular septum revealed less pronounced differences between 6J and 6N mice (Supplemental Figures S7B and S7C).

The macroscopic appearance of a nutmeg-colored liver reflecting venous congestion occurred in 50% of 6N mice after 4 weeks but not in 6J mice (Figure 3A). Likewise, microscopic signs of hepatic venous congestion were significantly more abundant in 6N compared with 6J mice (Figures 3B and 3C). Given that venous congestion is appreciated as a clinical symptom of heart failure (HF), a receiver-operating characteristics curve analysis was performed to calculate the accuracy for the identification of RHF-prone 6N mice by quantifying the

FIGURE 1 Right Ventricular Morphology and Function in 6J Mice Upon Pulmonary Artery Banding

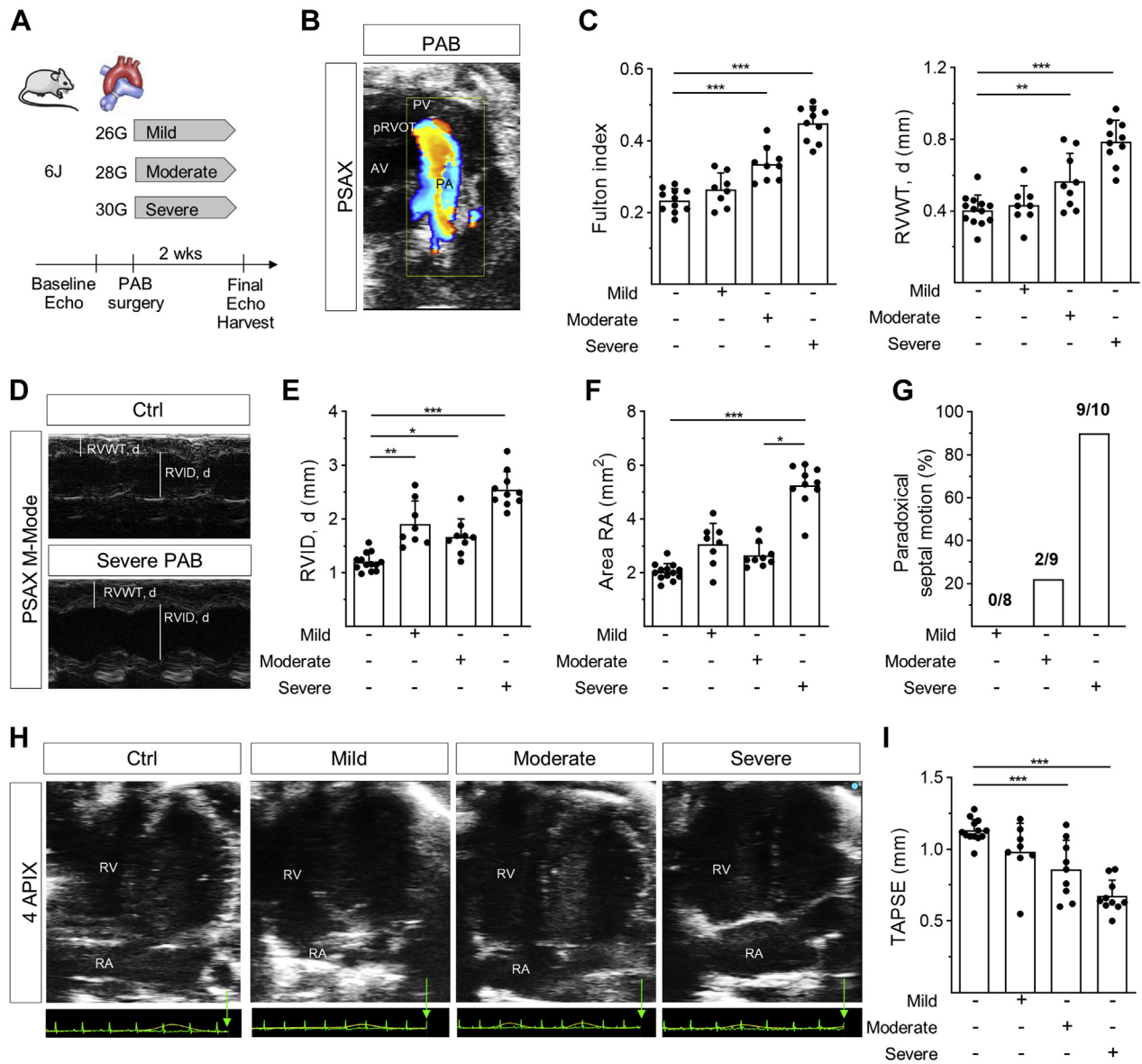
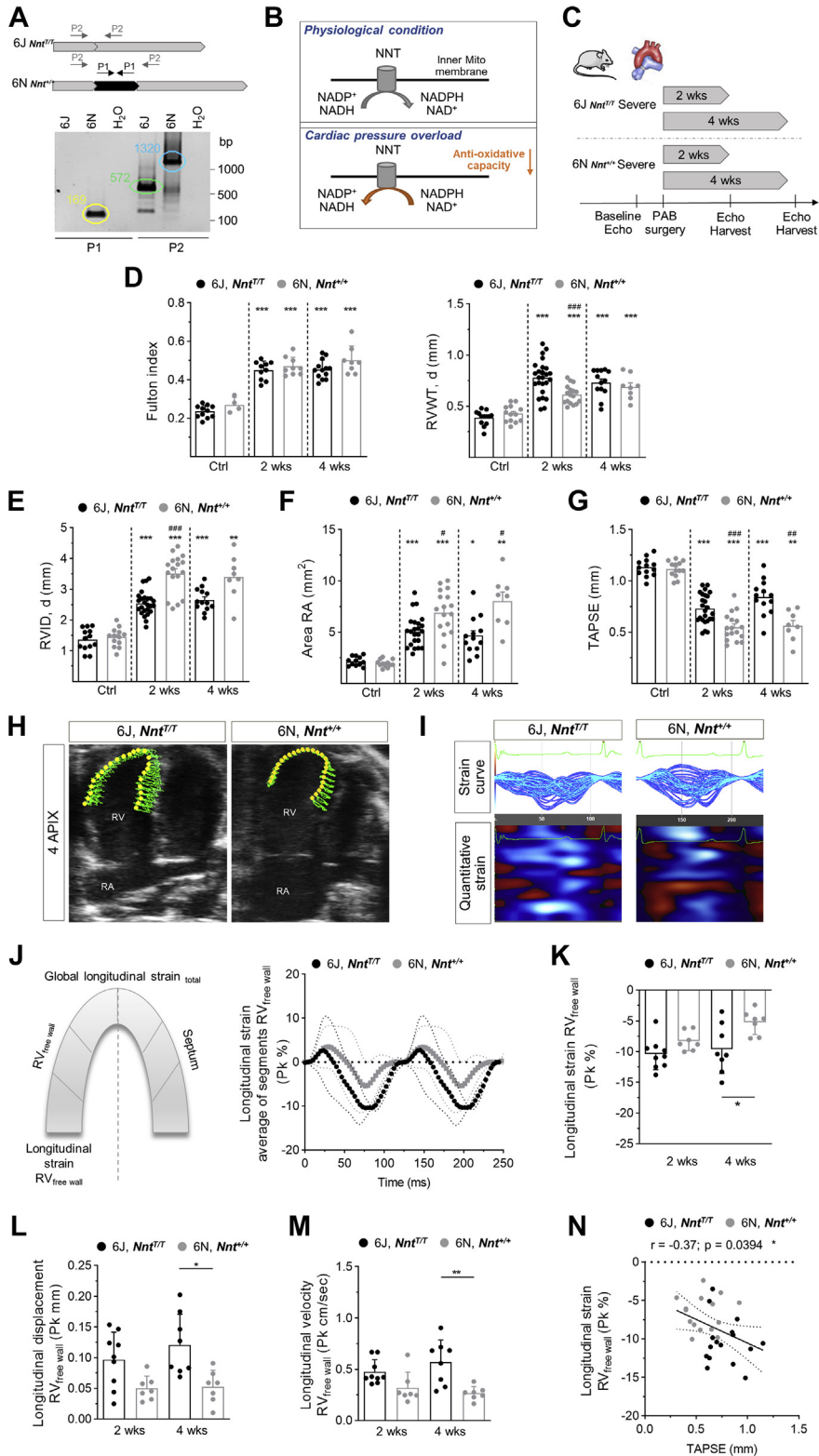


FIGURE 2 RV Function in 6J and 6N Mice Upon PAB



congestion-modified areas in liver sections (Figure 3D). It revealed that microscopic signs of venous congestion are appropriate to distinguish 6N mice, and a cutoff value of 21.5% with a sensitivity of 87.5% and a specificity of 75% and an area under the curve of 0.836 (95% CI: 0.62-1.00) for the congestion-modified area in liver sections was calculated. With this, 25% of 6J and 87.5% of 6N mice were identified as mice prone to RHF (Supplemental Figure S8). It is noteworthy that the extent of hepatic congestion showed a strong inverse correlation with TAPSE and a strong positive correlation with RA area (Figures 3E and 3F). The more severe phenotype of 6N mice was corroborated by the absence of mortality during the 4 weeks of PAB in 6J but not in 6N mice (Figure 3G).

RHF IN PRESSURE-OVERLOADED NNT-COMPETENT 6N MICE IS DISSOCIATED FROM STRUCTURAL REMODELING. Interestingly, the differences in RV function between 6J and 6N mice were not accompanied by a different degree of fibrosis (Figure 4A). This suggests that the occurrence of RHF is dissociated from the extent of RV fibrosis, which is supported by the fact that the extent of hepatic venous congestion did not correlate with RV fibrosis (Figure 4B). Likewise, and in accordance with RVWT and Fulton index, cardiomyocyte cross-sectional area did not differ between 6J and 6N mice upon 4 weeks of PAB (Figures 4C and 4D) and, like fibrosis, did not show a correlation with hepatic congestion (Figure 4F). Apart from fibrotic remodeling, capillary rarefaction has been frequently linked to RHF.^{27,28} Whereas the number of capillaries in 6J mice was restored after 4 weeks of PAB, in 6N mice after

4 weeks of PAB it was slightly decreased compared with the control 6N animals (Figures 4C and 4E).

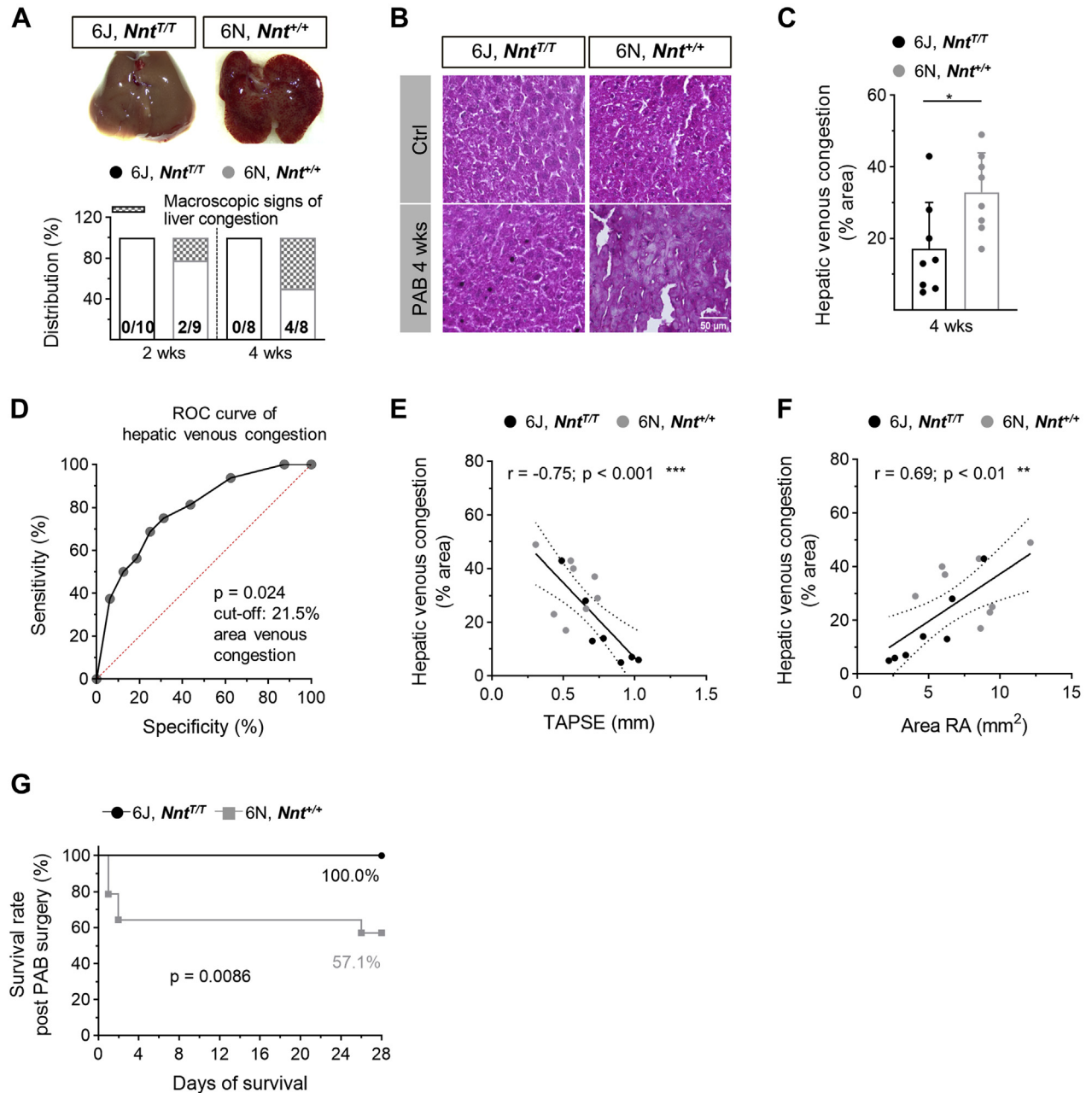
To assess the temporal development of RHF, functional and structural analyses after 1, 2, 4, and 6 weeks of PAB were performed in 6N mice (Figure 5A). Whereas RVID, RA area, TAPSE, and RV wall thickness were all significantly changed after 1 week of PAB compared with baseline (Figures 5B to 5E), RA area showed a further significant increase after 2 weeks compared with 1 week, but not thereafter, indicating that the development of RHF occurs early, between 1 and 2 weeks (Figure 5C). Corroborating this temporal phenotypic progress in 6N mice in particular after 1 week, hepatic venous congestion was also significantly more abundant after 2, 4, and 6 weeks compared with the 1-week time point (Figures 5F and 5G). In contrast, not only was the extent of RV fibrosis significantly higher after 2 weeks compared with 1 week, but it further increased until the 4-week timepoint (Figures 5H and 5I).

RHF IN PRESSURE-OVERLOADED NNT-COMPETENT 6N MICE IS MEDIATED BY OXIDATIVE STRESS. As described for the LV under pressure overload before,¹⁸ in our model, oxidative stress was more pronounced in RV tissue of 6N compared with 6J mice. The antioxidant enzyme PRX, which can form a dimer upon oxidation, is hyperoxidized to the sulfinic or sulfonic acid at cysteine residue Cys51 when exposed to high oxidative stress. This hyperoxidized form of PRX significantly increased in RV of 6N mice after 4 weeks of PAB, but not in 6J mice, consistent with the observations in the LV (Figures 6A and 6B). Accordingly, immunostaining for the DNA oxidation

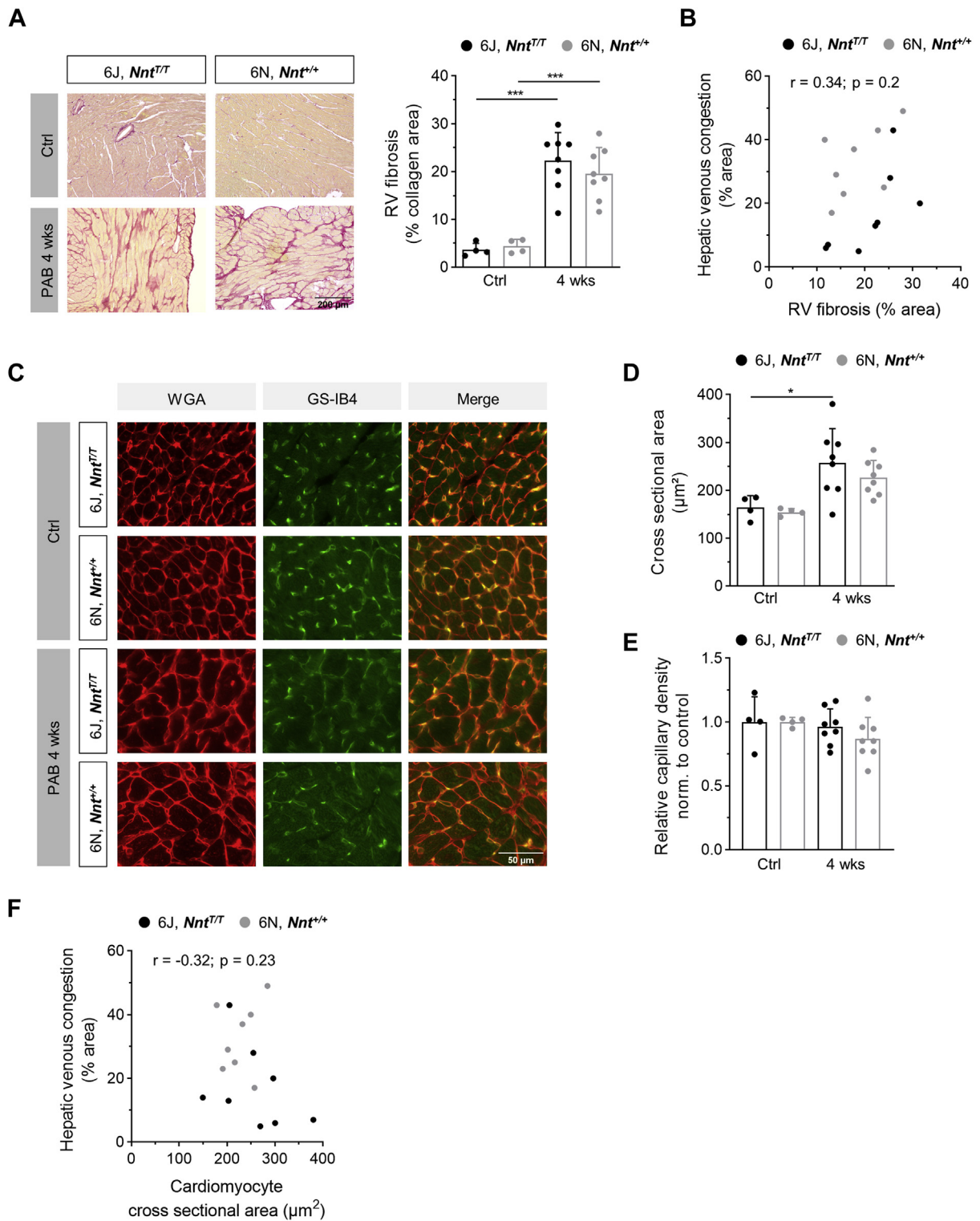
FIGURE 2 Continued

(A) Representative genotyping of 6J and 6N mice by specific amplification of the nicotinamide nucleotide transhydrogenase (*Nnt*). 6J mice harbor an in-frame 5 exon deletion leading to a loss of exon 7-11.²⁶ Primer pair 1 (PP1) is located within the coding sequence of exon 7-11, failing to be amplified in 6J mice. Primer pair 2 (PP2) is spanning exon 7-11, resulting in a truncated fragment in 6J mice compared with the wild type *Nnt* fragment amplified in 6N mice. (B) Schematic demonstration of NNT function. According to Nickel et al,¹⁸ the NNT switches from forward to reversed mode under cardiac pressure overload. (C) Schematic demonstration of experimental design. PAB was performed in 6J mice lacking the NNT (*Nnt^{fl/fl}*) and 6N mice expressing functional active NNT (*Nnt^{+/+}*). (D) RV hypertrophy as assessed by Fulton index ($n = 11/4/10/9/13/8$ mice) and diastolic RV wall thickness ($n = 13/13/25/17/13/8$ mice) was increased upon severe PAB after 2 and 4 weeks in 6J and 6N mice. Dilation of the RV (E) and the RA (F) was augmented in 6N compared with 6J mice upon 2 and 4 weeks of PAB ($n = 13/13/25/17/13/8$ mice). (G) RV function as assessed from TAPSE was more impaired in 6N vs 6J mice upon PAB after 2 and 4 weeks ($n = 13/13/25/17/13/8$ mice). (H) Representative image of speckle tracking in 2-dimensional parasternal apical 4-chamber view for longitudinal strain analysis using Vevo strain analysis module in 6J and 6N upon PAB. (I) Strain curves (top) and corresponding quantitative strain analysis represented as heat map (bottom) of 6J and 6N mice. (J) Schematic description of sections used for analysis of longitudinal strain_{total} and strain RV_{free wall} (left). A strain curve was calculated for every segment. The average of strain curves (bold symbols) and the SEM (thin symbols) demonstrating deformation of RV free wall of 6J and 6N mice upon 4 weeks of PAB. One representative animal per group is shown. (K) Longitudinal strain of the RV free wall was significantly diminished in 6N compared with 6J mice upon 4 weeks of PAB. Pk = peak ($n = 9/7/8/7$ mice). (L) Longitudinal displacement and (M) velocity of the RV free wall was significantly decreased in 6N compared with 6J mice upon 4 weeks of PAB ($n = 9/7/8/7$ mice). (N) Longitudinal strain of the RV free wall negatively correlated with TAPSE reflecting RV systolic function ($n = 31$ mice). Statistical significance in D (Fulton index) and K to M was calculated with 1-way analysis of variance, in D (RVWT, d) to G with a marginal linear mixed effect model, followed by Bonferroni's post hoc test. For N, Pearson correlation was tested. * $P < 0.05$; ** $P < 0.01$; *** $P < 0.001$ compared with respective control; # $P < 0.05$; ## $P < 0.01$; ### $P < 0.001$ compared with corresponding 6J. Abbreviations as in Figure 1.

FIGURE 3 Characteristics of Right Heart Failure Upon PAB



(A) Macroscopic and (B and C) microscopic signs of venous congestion in livers were more pronounced in 6N compared with 6J mice upon 4 weeks of PAB (n = 8-14 mice). Representative images of livers upon PAB (A) after excision and (B) of liver sections stained with hematoxylin/eosin. Pale areas indicate damage caused by venous congestion. Scale bar = 50 μ m. (D) Receiver-operating characteristic (ROC) curve for the area of hepatic venous congestion (C) of 6J and 6N mice receiving a cutoff value of 21.5%. (E) TAPSE of 6J and 6N mice upon 4 weeks of PAB showed a significant negative correlation and (F) RA area showed a significant positive correlation with the extent of hepatic venous congestion as assessed in hematoxylin/eosin-stained liver sections (n = 15 mice). (G) Survival rate, excluding animals that died at the day of surgery, was lower within 4 weeks after PAB in 6N compared with 6J mice (n = 14/13 mice). Statistical significance in C was calculated with 2-tailed unpaired Student's *t*-test and in G with log-rank test. For E and F, Pearson correlation was tested. * $P < 0.05$; ** $P < 0.01$; *** $P < 0.001$. Abbreviations as in Figure 1.

FIGURE 4 RV Remodeling in 6J and 6N Mice Upon Pulmonary Artery Banding

Continued on the next page

product 8-OHdG in RV sections revealed higher levels of oxidative stress in 6N mice: The number of 8-OHdG-positive cardiomyocyte nuclei was significantly enhanced in 6N mice following 4 weeks of PAB, but not in 6J mice (Figures 6C and 6D), and the percentage of the area with 8-OHdG immunoreactivity in all nuclei was significantly higher in PAB-exposed 6N than in 6J mice (Figures 6E and 6F). Mitochondrial content as expressed by mitochondrial DNA copy number was slightly diminished after PAB to the same extent in both mouse strains (Figure 6G). Given that oxidative DNA damage can result in apoptotic cell death, TUNEL assay was performed to detect apoptotic DNA fragmentation. The number of TUNEL-positive nuclei was significantly increased in 6N mice upon 4 weeks of PAB compared with nonbanded 6N control mice, whereas no significant increase was observed in 6J mice (Figure 6H). Of note, apoptotic cell number showed a significant negative correlation with systolic RV function (Figure 6I), and a significant positive correlation with signs of venous congestion in the livers (Figure 6J), pointing toward apoptosis to be related to the severity of RHF. In corroboration of the pivotal role of ROS for RV function, treatment of mice with the mitochondrial antioxidant mitoTEMPO during 4 weeks of PAB improved systolic RV function (Figure 6K) and diminished venous congestion in particular in 6N mice (Figure 6L). The number of apoptotic nuclei was significantly more reduced in 6N compared with 6J mice upon mitoTEMPO administration (Figure 6M), substantiating the causal relation of oxidative stress with apoptosis.

SEVERE IMPAIRMENT OF RV FUNCTION OF LHF PATIENTS IS ASSOCIATED WITH OXIDATIVE STRESS. RV function of 21 patients with dilated cardiomyopathy of genetic and nongenetic origin (see Table 1) was assessed by echocardiography before HTx. Patients were classified into the 2 groups nRVF (n = 11) and iRVF (n = 10) according to TAPSE, with ≥ 16 mm defined as normal and ≤ 13 mm defined as severely impaired. The 2 patients in whom TAPSE was not available were assigned to nRVF based on

FAC >35 . The 2 groups exhibited significant differences in TAPSE and FAC (Figures 7A and 7B), but displayed equal systolic LV function reflected by LV ejection fraction (Figure 7C). Of note, PH was almost absent in nRVF patients, in contrast to the iRVF group, as indicated by mean PA pressure below 25 mm Hg and an elevated PA wedge pressure (Figures 7D and 7E). The iRVF group showed a combined precapillary and postcapillary PH with a substantial extent of precapillary hemodynamic impairment, as shown by a marked elevation in pulmonary vascular resistance, with only 20% of nRVF patients but 70% of iRVF patients above the threshold of $240 \text{ dyn} \cdot \text{sec} \cdot \text{cm}^{-5}$ (Figure 7F), and a significantly impaired RV-PA coupling (Figure 7G). Histological analyses revealed that RV collagen accumulation was not different between the 2 groups (Figure 7H). Similarly, cardiomyocyte cross-sectional area and capillary density was equal (Figures 7I to 7K). In accordance with the findings in mice following 4 weeks of severe PAB, oxidative DNA damage was significantly more pronounced in RV sections of patients with severely impaired RV function (Figure 7L), underlining the important role of oxidative stress in the RV.

DISCUSSION

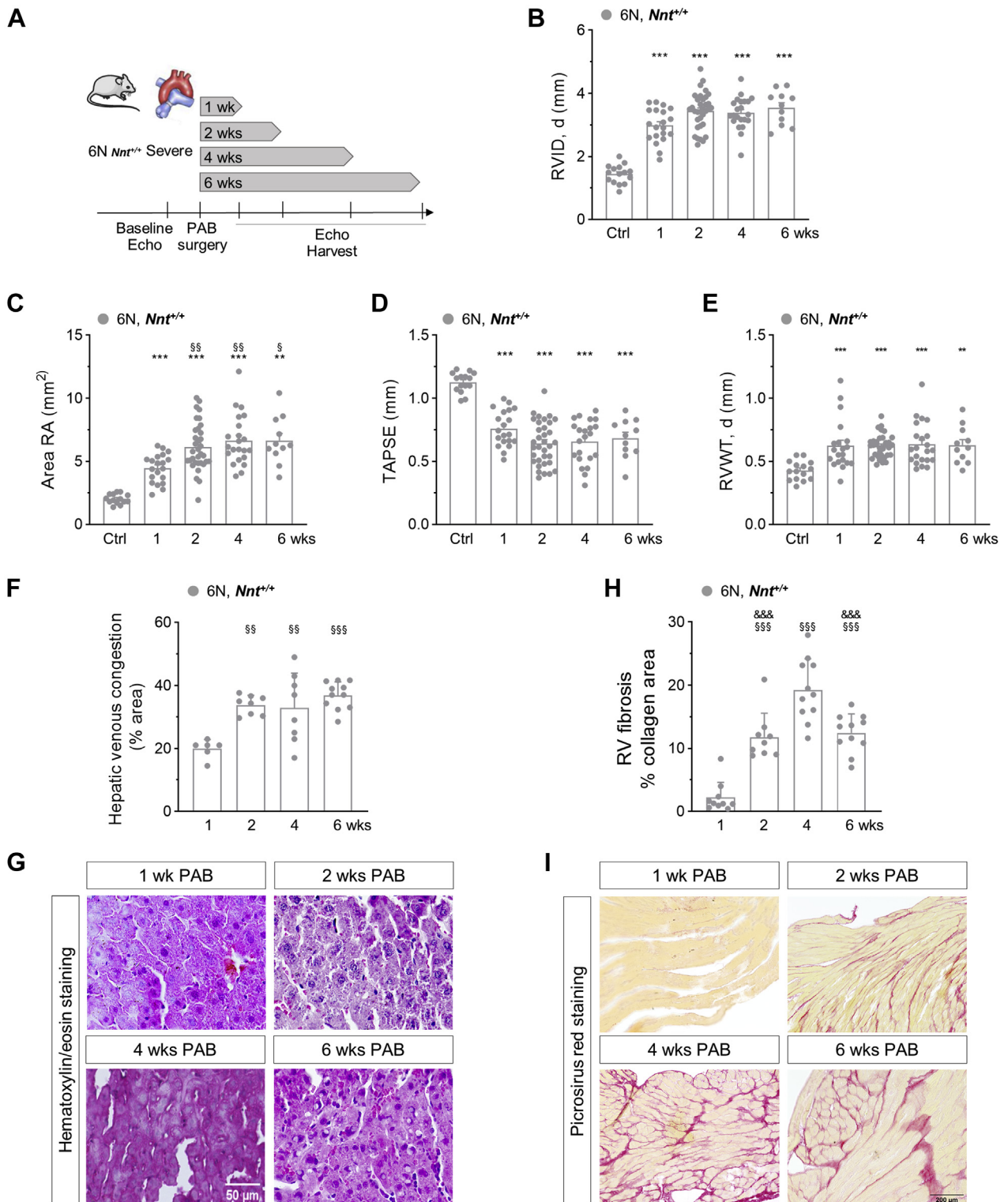
Our study demonstrates that the extent of RVH, dysfunction, and fibrosis is tightly linked to the degree of RV afterload. An important finding of our experiments is that during the transition from adaptive RV remodeling to failure, hypertrophy and fibrosis are dissociated from RV dilation and systolic function. Mechanistically, we disclose that mitochondria-generated ROS play a pivotal role for deterioration of RV function and the transition to RHF following pressure overload and might be causally related to a severe impairment of RV function in patients.

THE ROLE OF OXIDATIVE STRESS IN RHF. Given that the occurrence of RHF determines mortality of PAH patients, it is of utmost importance to identify the

FIGURE 4 Continued

(A) Representative images of picrosirius red stained RV sections (scale bar = 200 μm) and morphometric analysis of fibrotic area showing increased fibrosis in 6J and 6N mice upon PAB. (B) The extent of hepatic venous congestion did not correlate with RV fibrotic area in 6J and 6N mice upon 4 weeks of PAB (n = 16 mice). (C) Representative images of staining for cardiomyocyte cross-sectional area analysis using wheat germ agglutinin (WGA) and capillary density using isolectin of griffonia simplicifolia (GSI-B4). Scale bar = 50 μm . (D) Cross-sectional area of RV cardiomyocytes was not significantly different between 6J and 6N mice after 4 weeks of PAB. (E) Capillary density after 4 weeks of PAB in relation to the respective untreated animals of 6J and 6N mice shows slightly decreased density upon PAB in 6N compared with 6J mice. (F) The extent of hepatic venous congestion did not correlate with cardiomyocyte cross-sectional area in 6J and 6N mice upon 4 weeks of PAB (n = 16 mice). Statistical significance was calculated with 1-way analysis of variance followed by Bonferroni's post hoc test for A, D and E. n = 4/4/8/8 mice. For B and F statistical significance for Pearson correlation was tested. *P < 0.05; ***P < 0.001. Abbreviations as in Figure 1.

FIGURE 5 Temporal Development of RV Morphology, Function, and Failure in 6N Mice Upon PAB



molecular mechanisms that account for failing of the RV and the potential pathomechanistic targets, aiming to advance RV-directed therapies. Importantly, our study underscores the significant role of oxidative stress in the development of RHF. Analogous to LV pressure overload, NNT deficiency in 6J mice reduced ROS-induced alterations in the pressure overloaded RV in our experiments, which resulted in protection from RHF, as reflected by almost absent signs of hepatic venous congestion. This is in accordance with previous findings regarding oxidative stress in RHF, which showed that an SOD/catalase mimetic or stimulation of the antioxidative transcription factor nuclear factor E2-related factor 2 (Nrf2) improved RV function in experimental PAH models without affecting remodeling of the pulmonary vasculature.^{5,29} In another study, the mitochondrial antioxidant mitoQ induced only slight improvements in RV function in the PAB model in 6J mice,³⁰ which also matches our data on the application of mitoTEMPO in 6J mice. In contrast to 6J mice, RV function in 6N mice was profoundly improved by application of mitoTEMPO, which is an SOD mimetic that accumulates in mitochondria. This effect is most likely related not only to a decrease of mitochondrial superoxide, but also to a reduction of hydrogen peroxide levels via a mitoTEMPO-dependent attenuation of superoxide-induced ROS release, as described for this antioxidant before in pressure-overloaded LV.³¹ It has been hypothesized that the RV is particularly sensitive to oxidative stress because of impaired up-regulation of SOD2 compared with the LV,¹¹ which has been observed in experimental models of PAH and chronic nitric oxide deficiency.^{10,12} The disruption of antioxidant enzyme up-regulation can be caused by oxidative stress itself feeding a vicious cycle, which became clear in our experiment through lower mRNA expression levels of SOD2 in 6J and 6N mice upon PAB compared with control animals ([Supplemental Figure S9](#)).

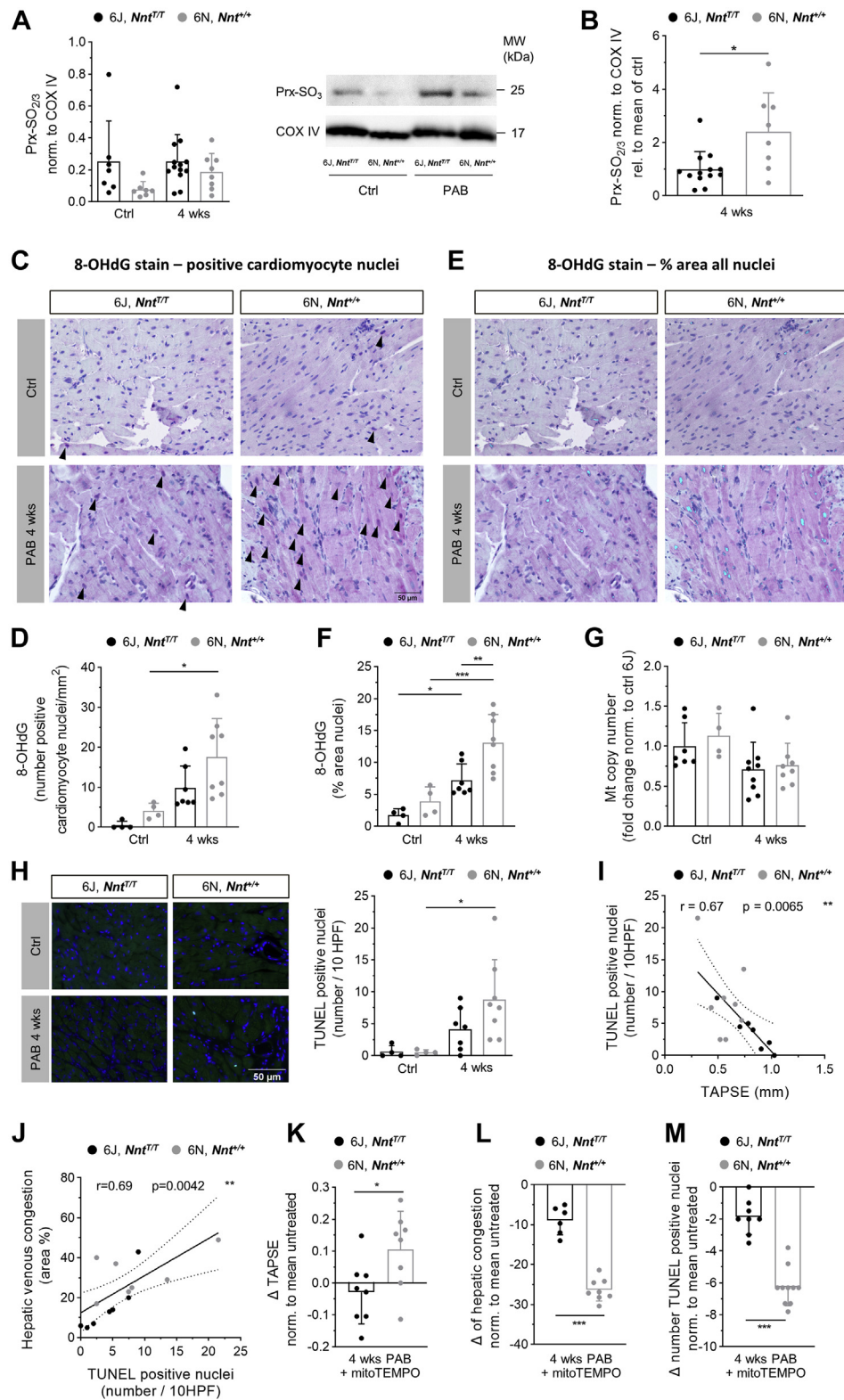
In the pressure overloaded LV, oxidative stress-mediated HF has been linked to fibrosis, necrosis,

and oxidative damage or adverse alterations of metabolic, antioxidant, and ion transport protein networks^{18,31,32} and is known to impair excitation contraction coupling (for review see Bertero and Maack²⁰). In addition, cardiomyocyte apoptosis has been linked to the progression of oxidative stress-related HF. Up-regulation of proteins involved in apoptosis after LV pressure overload was diminished in mice overexpressing human catalase in cardiomyocyte mitochondria.³² Undoubtedly, cardiomyocyte apoptosis is of relevance for LV dysfunction,^{33,34} and increased numbers of apoptotic cardiomyocytes have been detected in the RV of PAB-exposed rodents previously.³⁵⁻³⁷

THE ROLE OF RV FIBROSIS IN RHF. Enhanced interstitial collagen deposition has been extensively studied as a potential therapeutic target in HF, and it has been accepted to be causally related to dysfunction of the LV, in particular to diastolic dysfunction. In patients with heart failure with preserved ejection fraction (HFpEF), LV fibrosis has been shown to be strongly correlated to mortality.³⁸ Preclinical studies revealed that fibrosis is often associated with RVH and/or RVD in different animal models of PAH and RV pressure overload. It was shown that effective therapeutic approaches or genetic manipulations to alleviate PAH or RVD upon experimental PAB often go along with a reduction of RV fibrosis.^{5,6,39-44} Rain et al⁴⁵ applied PAB with 2 different degrees of stenosis to rats and showed that under severe constriction, not only did the percentage of collagen deposition in the RV increase, but also the ratio of collagen I to III increased, which accounted for enhanced myocardial stiffness.⁴⁵ However, a causal relationship for fibrosis in RHF remains elusive. Instead, this concept has been challenged during recent years: In a PAB mouse model with self-dissolving suture, RV fibrosis slowly reversed at a time point when RV function and hypertrophy were already fully normalized.⁴⁶ Furthermore, in the murine PAB model, galectin-3 knockout or inhibition and the antifibrotic agent pirfenidone attenuated RV

FIGURE 5 Continued

(A) Schematic demonstration of experimental design. PAB was performed in 6N mice expressing functional active NNT (*Nnt*^{+/+}) and final organ harvest was performed at different time points. (B) RVID, d, (C) RA area, (D) TAPSE, and (E) RVWT, d were assessed after 1, 2, 4, and 6 weeks of PAB and were significantly increased after 1 week compared with baseline. (C) Area RA was further increased after 2, 4, and 6 weeks compared with 1 week, respectively (n = 15/20/34/22/11 mice). (F) Hepatic venous congestion as assessed from hematoxylin/eosin-stained sections (G) was significantly higher after 2, 4, and 6 weeks compared with 1 week of PAB (n = 6/9/8/11 mice). (H) The extent of RV fibrosis as assessed from picrosirius red-stained sections (I) was highest after 4 weeks of PAB (n = 6/9/8/11 mice). Statistical significance for B to E was calculated with a marginal linear mixed effect model and for F and H with 1-way analysis of variance followed by Bonferroni's post hoc test. **P < 0.01; ***P < 0.001 compared with respective control; [§]P < 0.05; ^{§§}P < 0.01; ^{§§§}P < 0.001 compared with the 1-week time point; ^{§§§}P < 0.001 compared with the 4 week time point. Abbreviations as in [Figure 1](#).

FIGURE 6 Oxidative Stress-mediated Alterations in 6J and 6N Mice Upon Pulmonary Artery Banding

Continued on the next page

fibrosis, but did not significantly affect RV function,⁴⁷ despite the fact that galectin-3 was linked to the development of LHF and also to mortality and RVD in patients with PAH.⁴⁷ Our data, on the one hand, confirm the relation between enhanced afterload and collagen deposition during hypertrophic remodeling,^{9,45,48} but on the other hand, prove a dissociation between RHF and RV fibrosis. The same is true for hypertrophy, which is in accordance with other studies in RV and LV pressure overload.^{18,44} Given that in LV pressure overload comparing 6J and 6N mice, fibrosis correlated with systolic LV function,¹⁸ this dissociation of fibrosis and function might reflect a pivotal difference of RHF and LHF pathomechanisms.

THE EXPERIMENTAL MODEL OF PAB. The mouse model of PAB is widely used to study RV remodeling independently from pulmonary vascular disease. Our data point out that the experimental design is of pivotal importance for the outcome of the study. On the one hand, the stenosis grade determining the degree of afterload results in gradual increases in RVH and fibrosis and decline in systolic RV function, as shown before in rats.^{9,45,48} Thus, the age and body weight of the mice at the time point of PAB surgery and their growth curve during observation time is closely related to the degree of RV remodeling (Supplemental Figure S10), because the extent of stenosis is dependent on PA size. On the other hand, it becomes obvious that the 6J mouse strain is protected from developing RHF at least during the 4-week observation time of our study. The majority of

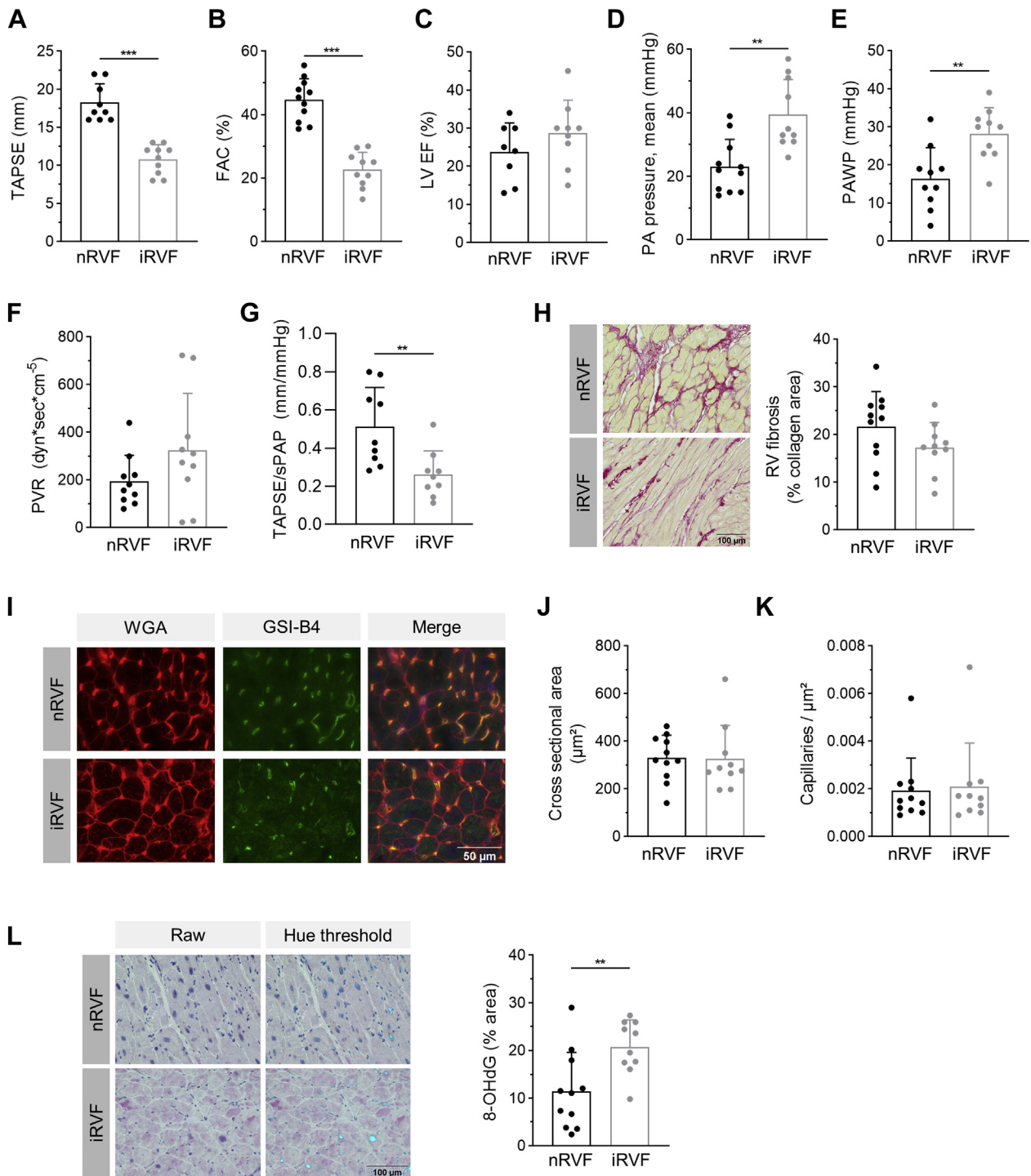
the published studies employing PAB in mice either use 6J mice or do not specify the exact strain of C57BL/6. Consequently, the impact of afterload for RHF is probably underestimated, and the statement that isolated RV pressure overload is insufficient to explain RHF⁵ is disproved. In contrast to rats, which develop a number of evident HF symptoms in the monocrotaline or PAB model,⁴⁹ mice exposed to RV pressure overload are more robust and hardly exhibit apparent changes in liver or body weight, amount of abdominal fluid, food consumption, general activity, or voluntary wheel running. However, we demonstrate in our PAB model that venous liver congestion strongly correlates with RV function and RA area (Figures 3E and 3F) and is an appropriate parameter reflecting RHF (Figure 3D). Furthermore, our data emphasize that a high-quality and careful evaluation of functional phenotyping is required for diligent generation of robust data. We observed that FAC as a common clinical parameter for systolic RV function is compromised in animals with maladaptive remodeling upon severe pressure overload because of paradoxical septal motion. To our knowledge, we for the first time provide RV strain analyses derived from echocardiography in a mouse model of right heart disease, which discloses that RV longitudinal strain correlates well with TAPSE.

STUDY LIMITATIONS. We cannot rule out that other differences between 6J and 6N mice contribute to the altered phenotype, such as a loss-of-function variant for the myosin light chain kinase 3 in 6N mice.⁵⁰ Furthermore, we have not investigated whether

FIGURE 6 Continued

Amount of hyperoxidized peroxiredoxin (Prx-SO_{2/3}) in RV tissue normalized to protein expression of cyclooxygenase IV (COX IV) (A) was increased in 6N but not in 6J mice upon 4 weeks of PAB (n = 7/7/13/8 mice), and (B) the increase was significantly higher in 6N than in 6J mice as assessed by immunoblot (n = 13/8 mice). Oxidative DNA modifications as reflected by immunoreactivity for 8-hydroxydeoxyguanosin (8-OHdG) were (C and D) significantly increased in nuclei of cardiomyocytes upon 4 weeks of PAB compared with untreated in 6N mice, but not in 6J mice, and (E and F) were significantly more abundant in total nuclei of RV sections of 6N compared with 6J mice upon PAB (n = 4/4/7/8 mice). Arrowheads in C indicate cardiomyocyte nuclei, with 8-OHdG immunoreactivity in purple. Light blue color in E indicates immunoreactivity for 8-OHdG marked with ImageJ hue threshold analysis. Scale bar = 50 μm. (G) Mitochondrial (mt) copy number was slightly decreased upon PAB to the same extent in 6J and 6N mice (n = 7/4/9/8 mice). (H) Number of apoptotic nuclei calculated per 10 high-power fields (HPF) (40× magnification) as revealed from TUNEL staining was significantly increased in RV sections of 6N mice after 4 weeks of PAB, but not in 6J mice (n = 4/4/7/8 mice). Representative images of TUNEL-stained RV sections. Blue = DAPI; bright green = TUNEL positive. Scale bar = 50 μm. (I) Number of TUNEL positive nuclei show a mild linear negative correlation with systolic RV function (TAPSE) in 6J and 6N mice upon PAB. (J) Extent of histological signs of hepatic venous congestion shows a mild linear correlation with number of TUNEL-positive nuclei in 6J and 6N mice upon PAB. (K) Alteration of TAPSE after 4 weeks of PAB and treatment with mitoTEMPO in relation to the respective untreated PAB animals was significantly different in 6N compared with 6J mice (n = 8/8). (L) Reduction of areas with signs of venous congestion in livers after 4 weeks of PAB and treatment with mitoTEMPO in relation to the respective untreated PAB animals was significantly higher in 6N compared with 6J mice (n = 6/8). (M) Reduction of the number of TUNEL-positive nuclei in RV sections in mitoTEMPO-treated animals related to untreated mice upon 4 weeks of PAB was significantly higher in 6N compared with 6J mice (n = 8/10). Statistical significance was calculated with Kruskal-Wallis test followed by Dunn's multicomparison test for A, with 1-way ANOVA followed by Bonferroni's post hoc test for D to H, with Mann-Whitney U test for B and M, with 2-tailed unpaired Student's t-test for K and L, and tested for Pearson correlation for I and J. *P < 0.05; **P < 0.01; ***P < 0.001. Abbreviations as in Figure 1.

FIGURE 7 Remodeling and Oxidative Damage in RV Tissue of Patients With Dilated Cardiomyopathy Before Heart Transplantation



Continued on the next page

oxidative stress is causally related to cardiomyocyte apoptosis, nor have we examined whether apoptosis accounts for deterioration of RV function in our model. Further mechanistic investigations need to follow to clarify the causal role and significance of these phenomena. We have not addressed other subcellular mechanisms that are probably affected by enhanced oxidative stress, such as substrate metabolism and sarcomere integrity. Another constraint of this study is the fact that the patient cohort does not perfectly match the experimental model. End-stage LHF patients most commonly develop RVD because of postcapillary PH and/or humoral mediators, whereas the PAB model resembles precapillary PH.

CONCLUSIONS

Our data provide evidence for a pivotal role of oxidative stress for the development of RHF. We disclose important phenotypic differences between 6J and 6N mice under RV pressure overload, most likely caused by the deficiency of the mitochondrial transhydrogenase NNT in 6J mice, which indicates that 6J mice are inappropriate to use when studying mechanisms of RHF following pressure overload. Our study furthermore confirms a dependency of RVH and RV fibrosis with the extent of afterload, and demonstrates an independency of RV function and RHF from structural remodeling.

ACKNOWLEDGMENTS The authors thank Désirée Gerdes, Anna Hamker, André Grafe, and Caroline Stanasiuk for expert technical assistance and Fenja Ricarda Pust for performing experiments.

FUNDING SUPPORT AND AUTHOR DISCLOSURES

This work was supported by the Deutsche Forschungsgemeinschaft, Bonn, Germany (RU 1678/3-3 to Dr Rudolph), by the Deutsche

Stiftung für Herzforschung, Frankfurt a.M., Germany (F/ 48/ 20 to Drs Müller and Klinke) and by FoRUM, Bochum, Germany (F991R-21 to Drs Rudolph and Klinke). The authors have reported that they have no relationships relevant to the contents of this paper to disclose.

ADDRESS FOR CORRESPONDENCE: Dr Anna Klinke, Clinic for General and Interventional Cardiology/Angiology, Herz- und Diabeteszentrum NRW, University Hospital, Ruhr Universität Bochum, Georgstrasse 11, 32545 Bad Oeynhausen, Germany. E-mail: aklinke@hdz-nrw.de.

PERSPECTIVES

COMPETENCY IN MEDICAL KNOWLEDGE: The understanding of pathomechanisms underlying RHF development is of utmost importance to advance diagnosis and therapy and to alleviate morbidity and mortality. We show that RV hypertrophy and RV fibrosis are not necessarily associated with the occurrence and severity of RHF, which may be of relevance for clinical diagnostics, prognostics, and decision-making.

TRANSLATIONAL OUTLOOK: Therapeutic options to treat RHF remain scarce. Currently, pharmacological agents that directly target the failing RV are missing. With our findings we provide detailed insight to the progress of RV hypertrophy and remodeling upon increasing afterload and to mechanistic patterns of the transition of RV remodeling to failure. We provide evidence that oxidative stress can be causally related to the development of RHF. This encourages the initiation of clinical studies in patients at risk of developing RHF testing treatment strategies that reduce oxidative stress or induce antioxidant pathways in cardiomyocytes.

FIGURE 7 Continued

Patients with dilated cardiomyopathy were divided into 2 groups with normal systolic right ventricular function (nRVF) and severely impaired right ventricular function (iRVF), exhibiting significant differences in (A) TAPSE (n = 9/10), (B) fractional area change (FAC) (n = 11/10), (D) mean pulmonary arterial (PA) pressure (n = 11/10), and (E) pulmonary artery wedge pressure (PAWP) (n = 11/10). (C) Systolic LV ejection fraction was reduced without differences between the 2 groups (n = 8/9). (F) Pulmonary vascular resistance (PVR) was markedly increased in iRVF patients (n = 11/10). (G) RV-PA coupling reflected by the ratio of TAPSE to systolic pulmonary artery pressure (sPAP) was significantly impaired in iRVF patients (n = 9/9). (H) Percentage of fibrotic area as assessed from picrosirius red staining (scale bar = 100 μ m) was not different in RV of nRVF and iRVF patients (n = 11/10). (I) Representative images of RV sections stained for cardiomyocyte cross-sectional area analysis using wheat germ agglutinin (WGA) and capillary density using isolectin of griffonia simplicifolia (GSI-B4). Scale bar = 50 μ m. (J) Cross-sectional area of cardiomyocytes was not different in RV of nRVF and iRVF patients (n = 11/10). (K) Capillary density was not different in RV of nRVF and iRVF patients (n = 11/10). (L) Oxidative DNA modifications as reflected by immunoreactivity for 8-hydroxydeoxyguanosin (8-OHdG) were significantly more abundant in nuclei of RV sections of patients with iRVF compared with nRVF (n = 11/10). Representative images, with purple nuclei indicating immunoreactivity for 8-OHdG (raw) and light blue color (hue threshold) indicates 8-OHdG immunoreactivity marked with ImageJ hue threshold analysis. Scale bar = 100 μ m. Statistical significance was calculated with unpaired Student's t-test for A to G and L and with Mann-Whitney U test for J and K. **P < 0.01; ***P < 0.001. Variation of n from nRVF/iRVF = 11/10 was caused by impossibility of assessment during echocardiography or catheterization for some of the parameters. Abbreviations as in Figure 1.

REFERENCES

- Konstam MA, Kiernan MS, Bernstein D, et al, for the American Heart Association Council on Clinical Cardiology, Council on Cardiovascular Disease in the Young, and Council on Cardiovascular Surgery and Anesthesia. Evaluation and management of right-sided heart failure: a scientific statement from the American Heart Association. *Circulation*. 2018;137:e578-e622.
- Reddy S, Bernstein D. Molecular mechanisms of right ventricular failure. *Circulation*. 2015;132:1734-1742.
- Veerou J, Mamazhakypov A, Rai N, et al. Effect of p53 activation on experimental right ventricular hypertrophy. *PLoS One*. 2020;15:e0234872.
- Heitmeier T, Sydykov A, Lukas C, et al. Altered proteasome function in right ventricular hypertrophy. *Cardiovasc Res*. 2020;116:406-415.
- Bogaard HJ, Natarajan R, Henderson SC, et al. Chronic pulmonary artery pressure elevation is insufficient to explain right heart failure. *Circulation*. 2009;120(20):1951-1960.
- Janssen W, Schymura Y, Novoyatleva T, et al. 5-HT2B receptor antagonists inhibit fibrosis and protect from RV heart failure. *Biomed Res Int*. 2015;2015:438403. <https://doi.org/10.1155/2015/438403>
- Kojonazarov B, Luitel H, Sydykov A, et al. The peroxisome proliferator-activated receptor β/δ agonist GW0742 has direct protective effects on right heart hypertrophy. *Pulm Circ*. 2013;3:926-935.
- Borgdorff MA, Koop AM, Bloks VW, et al. Clinical symptoms of right ventricular failure in experimental chronic pressure load are associated with progressive diastolic dysfunction. *J Mol Cell Cardiol*. 2015;79:244-253.
- Andersen S, Schultz JG, Andersen A, et al. Effects of bisoprolol and losartan treatment in the hypertrophic and failing right heart. *J Card Fail*. 2014;20:864-873.
- Redout EM, Wagner MJ, Zuidwijk MJ, et al. Right-ventricular failure is associated with increased mitochondrial complex II activity and production of reactive oxygen species. *Cardiovasc Res*. 2007;75:770-781.
- Schluter KD, Kutsche HS, Hirschhauser C, Schreckenberg R, Schulz R. Review on chamber-specific differences in right and left heart reactive oxygen species handling. *Front Physiol*. 2018;9:1799.
- Schreckenberg R, Rebelo M, Deten A, et al. Specific mechanisms underlying right heart failure: the missing upregulation of superoxide dismutase-2 and its decisive role in antioxidative defense. *Antioxid Redox Signal*. 2015;23:1220-1232.
- Nagendran J, Gurtu V, Fu DZ, et al. A dynamic and chamber-specific mitochondrial remodeling in right ventricular hypertrophy can be therapeutically targeted. *J Thorac Cardiovasc Surg*. 2008;136:168-178, 178.e1-e3.
- Borchi E, Bargelli V, Stillitano F, et al. Enhanced ROS production by NADPH oxidase is correlated to changes in antioxidant enzyme activity in human heart failure. *Biochim Biophys Acta*. 2010;1802:331-338.
- Manni ME, Rigacci S, Borchi E, et al. Monoamine oxidase is overactivated in left and right ventricles from ischemic hearts: an intriguing therapeutic target. *Oxid Med Cell Longev*. 2016;2016:4375418.
- Phillips D, Aponte AM, Covian R, Neufeld E, Yu ZX, Balaban RS. Homogenous protein programming in the mammalian left and right ventricle free walls. *Physiol Genomics*. 2011;43:1198-1206.
- Brown DA, Perry JB, Allen ME, et al. Expert consensus document: Mitochondrial function as a therapeutic target in heart failure. *Nat Rev Cardiol*. 2017;14:238-250.
- Nickel AG, von Hardenberg A, Hohl M, et al. Reversal of mitochondrial transhydrogenase causes oxidative stress in heart failure. *Cell Metab*. 2015;22:472-484.
- Kohlhaas M, Maack C. Interplay of defective excitation-contraction coupling, energy starvation, and oxidative stress in heart failure. *Trends Cardiovasc Med*. 2011;21:69-73.
- Bertero E, Maack C. Calcium signaling and reactive oxygen species in mitochondria. *Circ Res*. 2018;122:1460-1478.
- Freeman HC, Huggill A, Dear NT, Ashcroft FM, Cox RD. Deletion of nicotinamide nucleotide transhydrogenase: a new quantitative trait locus accounting for glucose intolerance in C57BL/6J mice. *Diabetes*. 2006;55:2153-2156.
- Toye AA, Lippiat JD, Proks P, et al. A genetic and physiological study of impaired glucose homeostasis control in C57BL/6J mice. *Diabetologia*. 2005;48:675-686.
- Zacchigna S, Paldino A, Falcão-Pires I, et al. Towards standardization of echocardiography for the evaluation of left ventricular function in adult rodents: a position paper of the ESC Working Group on Myocardial Function. *Cardiovasc Res*. 2021;117:43-59.
- Kohut A, Patel N, Singh H. Comprehensive echocardiographic assessment of the right ventricle in murine models. *J Cardiovasc Ultrasound*. 2016;24:229-238.
- Shah M, Phillips MR, Quintana M, Stupp G, McLean SE. Echocardiography allows for analysis of pulmonary arterial flow in mice with congenital diaphragmatic hernia. *J Surg Res*. 2018;221:35-42.
- Huang TT, Naeemuddin M, Elchuri S, et al. Genetic modifiers of the phenotype of mice deficient in mitochondrial superoxide dismutase. *Hum Mol Genet*. 2006;15:1187-1194.
- Sutendra G, Dromparis P, Paulin R, et al. A metabolic remodeling in right ventricular hypertrophy is associated with decreased angiogenesis and a transition from a compensated to a decompensated state in pulmonary hypertension. *J Mol Med (Berl)*. 2013;91:1315-1327.
- Potus F, Ruffenach G, Dahou A, et al. Downregulation of MicroRNA-126 contributes to the failing right ventricle in pulmonary arterial hypertension. *Circulation*. 2015;132(10):932-943.
- Redout EM, van der Toorn A, Zuidwijk MJ, et al. Antioxidant treatment attenuates pulmonary arterial hypertension-induced heart failure. *Am J Physiol Heart Circ Physiol*. 2010;298:H1038-H1047.
- Pak O, Scheibe S, Esfandiary A, et al. Impact of the mitochondria-targeted antioxidant MitoQ on hypoxia-induced pulmonary hypertension. *Eur Respir J*. 2018;1701024. <https://doi.org/10.1183/13993003.01024-2017>
- Dey S, DeMazumder D, Sidor A, Foster DB, O'Rourke B. Mitochondrial ROS drive sudden cardiac death and chronic proteome remodeling in heart failure. *Circ Res*. 2018;123:356-371.
- Dai DF, Hsieh EJ, Liu Y, et al. Mitochondrial proteome remodelling in pressure overload-induced heart failure: the role of mitochondrial oxidative stress. *Cardiovasc Res*. 2012;93:79-88.
- Wencker D, Chandra M, Nguyen K, et al. A mechanistic role for cardiac myocyte apoptosis in heart failure. *J Clin Invest*. 2003;111:1497-1504.
- Foo RS, Mani K, Kitsis RN. Death begets failure in the heart. *J Clin Invest*. 2005;115:565-571.
- Braun MU, Szalai P, Strasser RH, Borst MM. Right ventricular hypertrophy and apoptosis after pulmonary artery banding: regulation of PKC isozymes. *Cardiovasc Res*. 2003;59:658-667.
- Nielsen EA, Sun M, Honjo O, Hjortdal VE, Redington AN, Friedberg MK. Dual endothelin receptor blockade abrogates right ventricular remodeling and biventricular fibrosis in isolated elevated right ventricular afterload. *PLoS One*. 2016;11:e0146767.
- Ramos SR, Pielles G, Sun M, Slorach C, Hui W, Friedberg MK. Early versus late cardiac remodeling during right ventricular pressure load and impact of preventive versus rescue therapy with endothelin-1 receptor blockers. *J Appl Physiol (1985)*. 2018;124:1349-1362.
- Garg P, Assadi H, Jones R, et al. Left ventricular fibrosis and hypertrophy are associated with mortality in heart failure with preserved ejection fraction. *Sci Rep*. 2021;11:617.
- Boehm M, Novoyatleva T, Kojonazarov B, et al. Nitric oxide synthase 2 induction promotes right ventricular fibrosis. *Am J Respir Cell Mol Biol*. 2019;60(3):346-356.
- Egemnazarov B, Crnkovic S, Nagy BM, Olschewski H, Kwapiszewska G. Right ventricular fibrosis and dysfunction: actual concepts and common misconceptions. *Matrix Biol*. 2018;68:69:507-521.
- Kojonazarov B, Novoyatleva T, Boehm M, et al. P38 mapk inhibition improves heart function in pressure-loaded right ventricular hypertrophy. *American Journal of Respiratory Cell and Molecular Biology*. 2017;57(5):603-614.
- Gomez-Arroyo J, Sakagami M, Syed AA, et al. Iloprost reverses established fibrosis in experimental right ventricular failure. *Eur Respir J*. 2015;45(2):449-462.

43. Budas GR, Boehm M, Kojonazarov B, et al. ASK1 inhibition halts disease progression in pre-clinical models of pulmonary arterial hypertension. *Am J Respir Crit Care Med*. 2018;197(3):373-385.
44. Boehm M, Tian X, Ali MK, et al. Improving right ventricular function by increasing BMP signaling with FK506. *Am J Respir Cell Mol Biol*. 2021;65(3):272-287.
45. Rain S, Andersen S, Najafi A, et al. Right ventricular myocardial stiffness in experimental pulmonary arterial hypertension: relative contribution of fibrosis and myofibril stiffness. *Circ Heart Fail*. 2016;9:e002636.
46. Boehm M, Tian X, Mao Y, et al. Delineating the molecular and histological events that govern right ventricular recovery using a novel mouse model of PA de-banding. *Cardiovasc Res*. 2020;116(10):1700-1709.
47. Crnkovic S, Egemnazarov B, Damico R, et al. Disconnect between fibrotic response and right ventricular dysfunction. *Am J Respir Crit Care Med*. 2019;199(12):1550-1560.
48. Andersen S, Schultz JG, Holmboe S, et al. A pulmonary trunk banding model of pressure overload induced right ventricular hypertrophy and failure. *J Vis Exp*. 2018;141:e58050. <https://doi.org/10.3791/58050>
49. Omura J, Habbout K, Shimauchi T, et al. Identification of long noncoding RNA H19 as a new biomarker and therapeutic target in right ventricular failure in pulmonary arterial hypertension. *Circulation*. 2020;142:1464-1484.
50. Williams JL, Paudyal A, Awad S, et al. Mylk3 null C57BL/6N mice develop cardiomyopathy, whereas Nnt null C57BL/6J mice do not. *Life Sci Alliance*. 2020;3(4):e201900593.

KEY WORDS oxidative stress, pressure overload, pulmonary artery banding, reactive oxygen species, right heart failure

APPENDIX For an expanded Methods section and supplemental figures, please see the online version of this paper.